High-fidelity control of spin ensemble dynamics via artificial intelligence: from quantum computing to NMR spectroscopy and imaging

Manu Veliparambil Subrahmanian[a], KowsalyaDevi Pavuluri[b], Cristina Olivieri [iD][a] and Gianluigi Veglia [iD][a,c,*]

[a]Department of Biochemistry, Molecular Biology & Biophysics, University of Minnesota, Minneapolis, MN 55455, USA
[b]Department of Radiology, Mayo Clinic, Rochester, MN 55905, USA
[c]Department of Chemistry, University of Minnesota, Minneapolis, MN 55455, USA
*To whom correspondence should be addressed: Email: vegli001@umn.edu
Edited By: Ian Wilson.

Abstract

High-fidelity control of spin ensemble dynamics is essential for many research areas, spanning from quantum computing and radio-frequency (RF) engineering to NMR spectroscopy and imaging. However, attaining robust and high-fidelity spin operations remains an unmet challenge. Using an evolutionary algorithm and artificial intelligence (AI), we designed new RF pulses with customizable spatial or temporal field inhomogeneity compensation. Compared with the standard RF shapes, the new AI-generated pulses show superior performance for bandwidth, robustness, and tolerance to field imperfections. As a benchmark, we constructed a spin entanglement operator for the weakly coupled two-spin-1/2 system of $^{13}CHCl_3$, achieving high-fidelity transformations under multiple inhomogeneity sources. We then generated band-selective and ultra-broadband RF pulses typical of biomolecular NMR spectroscopy. When implemented in multipulse NMR experiments, the AI-generated pulses significantly increased the sensitivity of medium-size and large protein spectra relative to standard pulse sequences. Finally, we applied the new pulses to typical imaging experiments, showing a remarkable tolerance to changes in the RF field. These AI-generated RF pulses can be directly implemented in quantum information, NMR spectroscopy of biomolecules, magnetic resonance imaging techniques for in vivo and materials sciences.

Keywords: artificial intelligence, evolutionary algorithm, RF pulse design, NMR, MRI

Significance Statement:

High-fidelity control of spin ensemble dynamics is at the foundation of many disciplines. Developing radio-frequency (RF) pulses that accomplish this task is an open challenge. We combined an evolutionary algorithm and artificial intelligence to design new RF pulse shapes with customizable fidelity and high compensation for external inhomogeneities. Our method lays the groundwork for developing new experiments at high and ultra-high NMR fields for spectroscopy and imaging techniques, impacting structural biology, biomedicine, and material sciences.

Introduction

High-fidelity control of quantum spin systems is at the foundation of many applications such as quantum computing, coherent and optical spectroscopies, NMR, and MRI (1–5). Spin operations such as excitation, inversion, refocusing, etc., are central to these techniques and are achieved by applying radio-frequency (RF) pulses of finite length and amplitude. However, the RF and external field inhomogeneities and finite pulse length effects make the coherent manipulation of spin ensemble dynamics challenging (6). In the experimental implementation of quantum computing, inhomogeneities affect the experimental fidelity of quantum gates, on-demand entangled state generation, and coherent control (1, 7, 8). These experimental errors also affect NMR and MRI at high and ultra-high magnetic fields as they require high-fidelity levels for coherent and high-efficiency control of heterogeneous spin ensembles (9, 10). Moreover, these imperfections accumulate in multipulse experiments, leading to low-fidelity operations and sizable signal losses (11). Although advanced computational techniques have been instrumental for designing compensated RF pulses such as composite, adiabatic, and numerically optimized pulses (6, 12–18, 19, 20–29), high- and ultra-high–field NMR and MRI spectroscopy require RF pulses with larger bandwidths, higher fidelity, and compensation for instrumental inhomogeneities. Here, we introduce a novel strategy to achieve high-fidelity control of spin ensemble dynamics with a high-level compensation for inhomogeneity and offset effects, reaching a fidelity for several spin operations up to 0.99999. Instead of tuning RF amplitude and duration for a given pulse shape, we search the phase space and let an evolutionary algorithm generate a library of ~2,00,000 phase shapes with constant amplitude. We then

trained an artificial intelligence (AI) algorithm with this library to generate the optimal solution for a given problem. Searching the phase space enabled the algorithm to achieve optimal solutions and reach an operational fidelity of 0.9999. Our versatile approach enables the design of several spin operations for various applications, including quantum computing, biomolecular NMR spectroscopy, and MRI techniques.

Results and discussion
The architecture of the GENETICS-AI algorithm

To design high-fidelity RF pulses, we combined an evolutionary algorithm with AI into a modular software, GENErator of TrIply Compensated RF pulSes via Artificial Intelligence (GENETICS-AI). The overall architecture of GENETICS-AI is reported in Figure S1. The core module of the algorithm consists of a network of interconnected optimization routines, including an iterative forward search (IFSA) and iterative self-correcting algorithms (ISCA) (Figure S2). These routines search the RF phase space and generate an Optimal Phase Surface (OPS) library through an iterative evolution of the solutions. A neural network (PhaseNET) is trained on this library and predicts new RF shapes with customizable flip angles, bandwidth (BW) with a specified fidelity, RF inhomogeneity compensation, and operational fidelity (Figure S3). A standout feature of GENETICS-AI is the multiple bidirectional validations of each RF shape through the optimization network, where each solution is connected to its neighbor as a generator or corrector.

### High-fidelity spin entanglement using GENETICS-AI

The creation and preservation of high-fidelity spin entanglement are central to several quantum computing applications (30, 31) and are ideal for testing the performance of GENETICS-AI (32–35). A reliable physical implementation of entangling two quantum systems requires unitary operations, which compensate for instrumental inhomogeneity within the experimentally feasible range. For NMR, dipolar/scalar coupled heteronuclear spins with $I = \frac{1}{2}$ (such as ^{1}H and ^{13}C in ^{13}CHCl$_3$, Figure 1A) form a two-qubit (quantum bit) quantum computer. External field inhomogeneities and errors in determining the coupling constant lower the fidelity of unitary operations, affecting the faithful implementation of quantum gate or quantum state creation. To improve the fidelity of unitary operations, we used GENETICS-AI to create a robust entangling operator (GEN-Entangler) for the weakly coupled two-spin-1/2 system of ^{13}CHCl$_3$ (Figure 1A to E). Each pulse in GEN-Entangler is triply compensated (36) to minimize inhomogeneities of RF field ($\Delta\omega_1$), offset (Ω), and weak scalar coupling interactions (ΔJ). The modular nature of the GEN-Entangler makes it possible to individually customize the level of compensation for $\Delta\omega_1$, Ω, and ΔJ, conferring a higher level of control for the desired operation. The J-coupling compensation level is controlled by the number of spin-echo (SE) elements (n) in the entangler sequence. For $n = 1$, GEN-Entangler consists of a single SE element with three global pulses and a J-coupling compensation level up to ±10%. For $n = 2$, the tolerance increases to ±30% and for $n = 4$ to ±50% (Figure 1C). To test the performance of GEN-Entangler, we used a pulse sequence with $n = 2$ and inhomogeneity compensation levels of ±20% and ±2 kHz for $\Delta\omega_1$ and BW, respectively (Figure 1C and Table S1). We first created a $|\alpha\alpha\rangle$ pseudo-pure state (37) for the ^{13}C–^{1}H spin pair (Figure 1F). Starting from the $|\alpha\alpha\rangle$ state, we generated a maximally entangled state, $1/\sqrt{2}$ ($|\alpha\alpha\rangle + |\beta\beta\rangle$), between the ^{1}H and ^{13}C spins. Figure S4 shows

the representative ^{1}H NMR spectra of thermal equilibrium, $|\alpha\alpha\rangle$ and $1/\sqrt{2}$ ($|\alpha\alpha\rangle + |\beta\beta\rangle$) states created by a $\pi/2$ pulse with phase zero. As a metric for robustness, we simulated a 0.99 fidelity iso-surface of the quantum states obtained by GEN-Entangler with the simultaneous compensation of $\Delta\omega_1$, Ω, and ΔJ, and compared it with the corresponding iso-surface generated using a standard Controlled-NOT (C-NOT) gate entangler using rectangular pulses (Figure 1G). We then experimentally generated six entangled states by detuning the pulses calibrated for optimal values. The yellow outer iso-surface in Figure 1G represents the fidelity volume obtained with the GEN-Entangler for $n = 2$, while the inner red surface represents the fidelity volume corresponding to the standard C-NOT entangler. Considering the maximum levels of inhomogeneity for all three parameters, the fidelity volume obtained by GEN-Entangler is approximately 100 times larger than the corresponding rectangular shape pulse. For an iso-surface fidelity of 0.98, the volume ratio, V_{GEN}/V_{RECT}, increases to 200 times (Figure 1H), demonstrating that the new entangler has a significantly higher tolerance for experimental errors. Additionally, the GEN-Entangler sequence is ~62% shorter than the ΔJ compensated C-NOT gate sequence (38), offering an additional advantage in terms of time duration.

As an additional test, we generated high-fidelity broadband (BB) RF pulses with arbitrary flip angles. Generalizing BB operations for an arbitrary spin-flip angle is quite challenging, as it requires individual optimization for the desired final state (39). The BB pulses for arbitrary flip angle transitions generated by our algorithm are reported in Figure 2A and B. Remarkably, the neural network trained on this OPS library output BB RF with smooth phase shapes with a fidelity greater than 0.9999 for any flip angle. We then tested this RF pulse generator by creating a programmable single qubit quantum state creator and a quantum gate generator. The former assumes an initial state $|\alpha\rangle$, whereas the latter consists of a BB universal flipping operation. Notably, the duration of the pulses does not depend on the flip angle or spin state. This feature is critical for quantum computing as the fixed length of these pulses removes any inhomogeneity associated with changes in time duration. The Bloch sphere trajectories of selected pulse operations with various flip angles are shown in Figure 2C and D. For example, we created the RF pulse of a 113.5° flip angle, with a smooth shape and an average fidelity of 0.9999 over a bandwidth of 50 kHz (Figure 2E-F). These high-fidelity single-qubit operations and the GEN-Entangler form a complete set of operations for universal quantum computing (40). Taken together these results show that the newly AI-generated pulses can perform any spin operation with high compensation and fidelity.

GENETICS-AI pulses for NMR spectroscopy at high and ultra-high magnetic fields

A critical requirement for NMR spectroscopy at high and ultra-high magnetic fields is the uniform excitation, inversion, and refocusing of nuclear magnetization over a broader BW. With this in mind, we programmed GENETICS-AI to generate new universal $\pi/2$ and π pulses to be used for multidimensional biological NMR (41). Two prototypical GENETICS-AI $\pi/2$ and π pulses are shown in Figures S5 and S6. These new pulses cover a BW of 40 kHz with pulse lengths less than 300 μs, with a constant RF amplitude ($\omega_1 = \gamma B_1/2\pi$) of 25 kHz, and an average operational fidelity of 0.9999, outperforming the standard rectangular pulses. The comparison between the universal GENETICS-AI π pulses and the rectangular pulses for different BWs show that the latter pulses display a limited high-fidelity region (Figure S7A), while the former
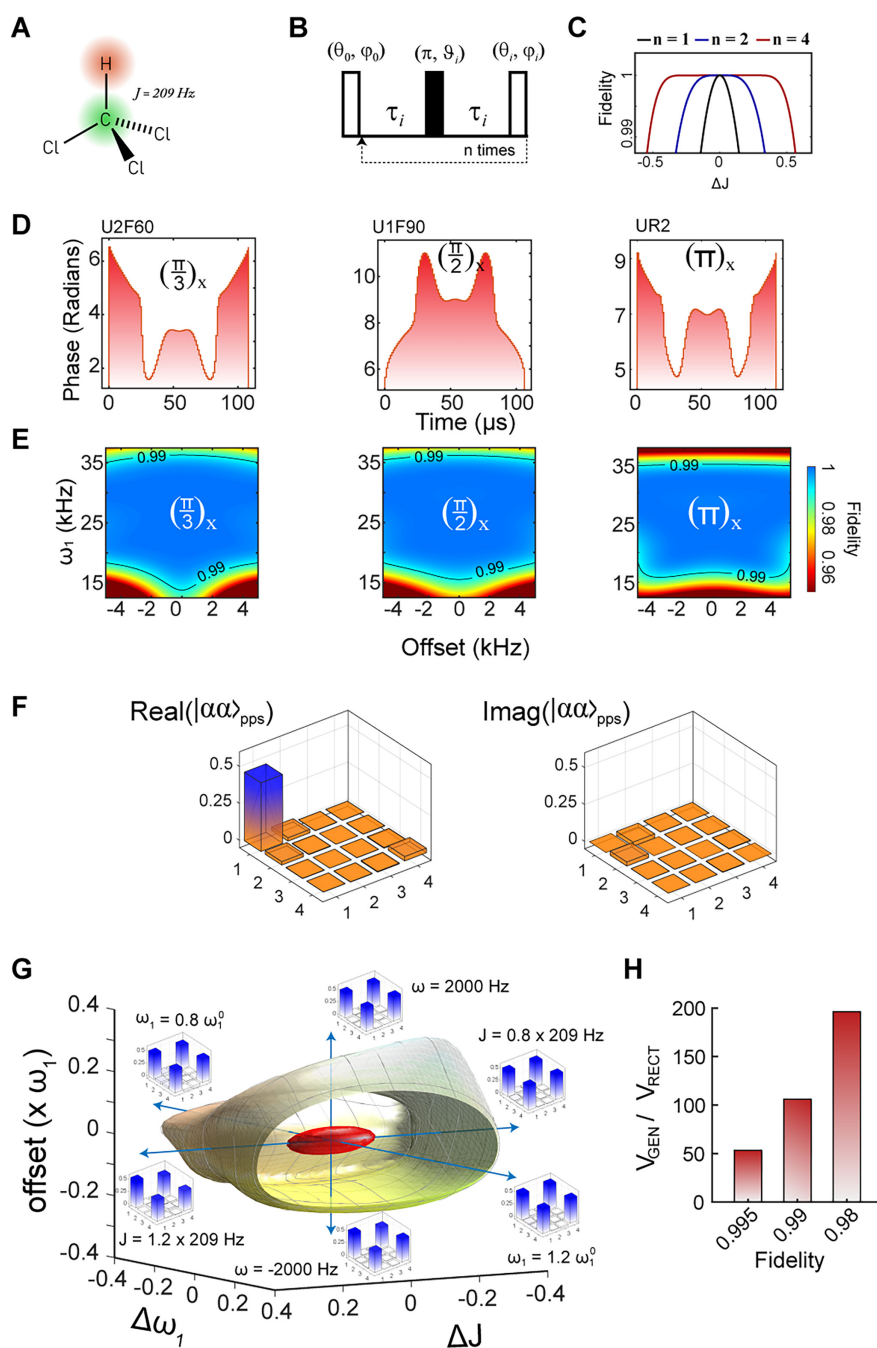
Figure 1. Generation of spin entanglement for ^{13}CHCl$_3$. (A) ^{13}CHCl$_3$ used for validating the GEN-Entangler pulse sequence. (B) GEN-Entangler pulse sequence. All the pulses are global for both ^{1}H and ^{13}C nuclei. Pulses and delay parameters for different values of n are given in Table S1. (C) J response curve of entanglement fidelity for $n = 1, 2,$ and 4. (D) and (E) RF shapes and corresponding fidelity profiles used for GEN-Entangler with $n = 2$. (F) Quantum state tomography for the real and imaginary part of the $|\alpha\alpha\rangle$ pseudo pure state created for ^{1}H and ^{13}C nuclear spins. (G) Simulated iso-surface at 0.99 fidelity for the entanglement created with $n = 2$ (outer surface—yellow) and standard C-NOT entangler with rectangular-shaped pulse (inner surface—red). The quantum state tomography results for simulated inhomogeneities on the 0.99 fidelity iso-surface for both extreme values of all three variables are shown in blue. (H) Fidelity volume fraction of entanglement created with GEN-Entangler (V_{GEN}) over standard C-NOT with rectangular pulses (V_{RECT}) for fidelities of 0.995, 0.99, and 0.98. All experiments were performed on a Bruker 600 MHz spectrometer at 300 K.

pulses show quite large fidelity regions, which extend to reach approximately 500 kHz for a pulse duration of 1360 μs (Figure S7B to E). To estimate the tolerance of these pulses to instrumental noise, we added random numerical noise to the phase and amplitude of a GENETICS-AI universal π pulse with a BW of 100 kHz and RF amplitude (ω_1) of 25 kHz and evaluated changes in its operational fidelity (Figure S8A to C). In the absence of noise, this pulse performs spin operations with a fidelity of 0.999. Upon addition of numerical noise with an amplitude of 5 kHz (20%), the fidelity drops by only 0.014 (i.e. 0.985), demonstrating a high tolerance to random noise sources. A similar scenario is predicted for errors in both amplitude and phase shape. Lastly, we assessed the performance of GENETICS-AI refocusing pulses against the best-performing pulses currently used for NMR and MRI. (16, 17, 36, 42–45) We compared their duration, operational BW, and average fidelity (Figure 3A, Table S2 and Table S3). The minimum fidelity
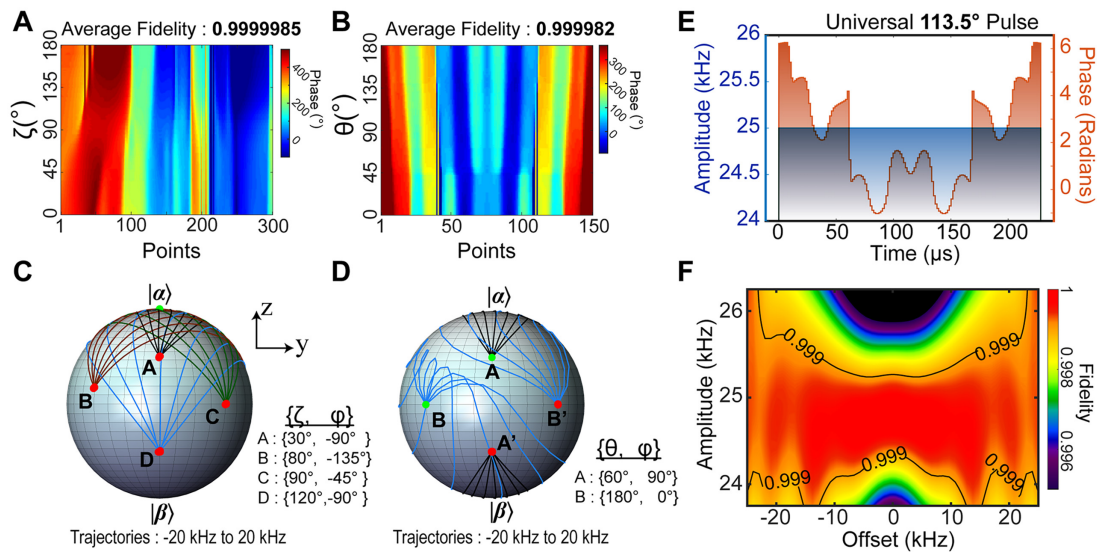
Figure 2. BB high-fidelity arbitrary flip angle pulses generated with GENETICS-AI. (A) OPS of a BB arbitrary state preparation with fidelity > 0.99999. The Y-axis represent the zenith angle (ζ) of the final state. The OPS was generated with an initial state fixed at $|\alpha\rangle$ and varying the ζ from 0 to π iteratively. The total nutation angle of the pulse was fixed at 8.68 π for all states. (B) OPS for arbitrary flipping operation with fidelity > 0.9999. The Y-axis represents the flip angle (θ) of the pulse. The OPS was created with θ as a target variable. The total nutation angle for the operation was fixed at 11.42 π. (C) Bloch sphere trajectories for the preparation of four different states (A, B, C, and D) using RF shapes from the OPS shown in (A). (D) Bloch sphere trajectories of two different flipping operations from A and A' to B and B' using RF shape from the OPS shown in (B). All trajectories are trimmed to show only 10% of the initial and final part. (E) RF shape of 113.5° universal flipping for a bandwidth of 50 kHz. The RF amplitude is constant (25 kHz). (F) 2D-fidelity response with offset and RF amplitude of the RF shape shown in (E).

for all GENETICS-AI pulses within the BW range is 0.99. For all the shapes analyzed, our new pulses show higher fidelity levels and shorter duration. Unlike the published shapes, our pulses are also time-optimal and customizable for any operational fidelity.

We then generated BB pulses that constitute the basic elements of many high-resolution NMR and MRI experiments. These pulses' homogeneity is critical for excitation, refocusing, and inversion operation in triple-resonance NMR pulse sequences for biomacromolecules (41). Additionally, BB pulses are used for excitation of active nuclei with large chemical shift breadth (e.g. ^{14}N, ^{19}F, ^{31}P, etc.) (46, 47), and are also essential for MRI in vivo and in materials science (48, 49). However, even in simple NMR experiments, the current pulses and pulse sequences generate artifacts (50) and suffer signal losses due to their low operational fidelity as well as the relaxation properties of the nuclear spin systems. Thanks to the flexibility of the Iterative Forward Search Algorithm (IFSA) and Iterative Self Correction Algorithm (ISCA) modules, we created customizable RF shapes for any operational fidelity. Several BB inversion pulses with fidelity varying from 0.9 to 0.99999 are represented in Figure S10A. Empirically, we found that the operational fidelity (F) of these RF pulses and the total nutation angles (Θ) follow this relationship:

$$\Theta \cong -S \cdot log(1 - F) + G, \qquad (1)$$

where S and G are the slope and intercept functions that depend on the BW, RF amplitude, and compensation level (Figure S10B). Equation 1 enables one to design and tune the inversion pulses with the desired fidelity level. This relationship also holds for universal π pulses as shown in Figure S10C to D. The performance of several inversion pulses with various operational fidelity is reported in (Figure S11A to B). Remarkably, we obtained a fidelity of 0.99999 for BB inversion pulse with a duration of 274 μs, BW of 100 kHz, and RF amplitude of 25 kHz. If the pulse length becomes a problem (as in the case of large macromolecular sys-

tems), this operation can be performed using a 57.5 μs pulse with a lower fidelity (e.g. 0.9), avoiding signal losses due to fast relaxation rates. It should be noted that the IFSA and ISCA optimization modules explore the phase space of any operation up to the limit imposed by the pulse shape digital resolution, i.e. the number of points (n) used to represent a given shape faithfully. To determine how the resolution influences a specific operation, we performed multiple optimizations of BB inversion pulses with different digital resolutions ($n = 16, 26, 50, 76,$ and 100). The progress for the IFSA/ISCA algorithm is shown in Figure S12. In this case, we observed a linear relationship between the total nutation angle, Θ, and BW, i.e. the increase of BW is constant for a unit change of the pulse length or amplitude (Figure S12A). The linearity holds up to maximum BW (BW_{max}) and increases with the digital resolution of the pulse shape (Figure S12B). However, at larger BW, this relationship is no longer linear, and the slope of the curve decreases, i.e. the RF power required to excite a specific BW increases. As the BW increases, the geometrical complexity of the specific shape increases, and more digital points are required. As an example, we generated ultra-BB universal π and inversion pulses and analyzed the Θ versus BW plot (Figure S12C) as well as their geometrical complexity (Figure S13). This analysis shows that achieving a BW of $20 \times \omega_1$ for a universal π operation requires an increase of the shape resolution of 2,000 digital points.

Moreover, we programmed GENETICS-AI to create ultra-BB pulses for exciting nuclei with extensive chemical shift breadth. Specifically, we designed universal $\pi/2$ and π pulses with a BW of $30 \times \omega_1$, which corresponds to 750 kHz for an RF amplitude, ω_1, of 25 kHz (Figure 3B and C). The pulse length of this ultra-BB pulse with 2,000 points generated was ~1.5 ms. To the best of our knowledge, this is the shortest universal pulse obtained for a 750 kHz BW. In theory, it is possible to generate ultra-BB pulses for a range of very large BWs (Figure S14). For instance, we designed an ultra-BB excitation pulse of 500 points to excite a BW of $22 \times \omega_1$ (Figure S15). This pulse is equivalent to an in-phase excitation BW
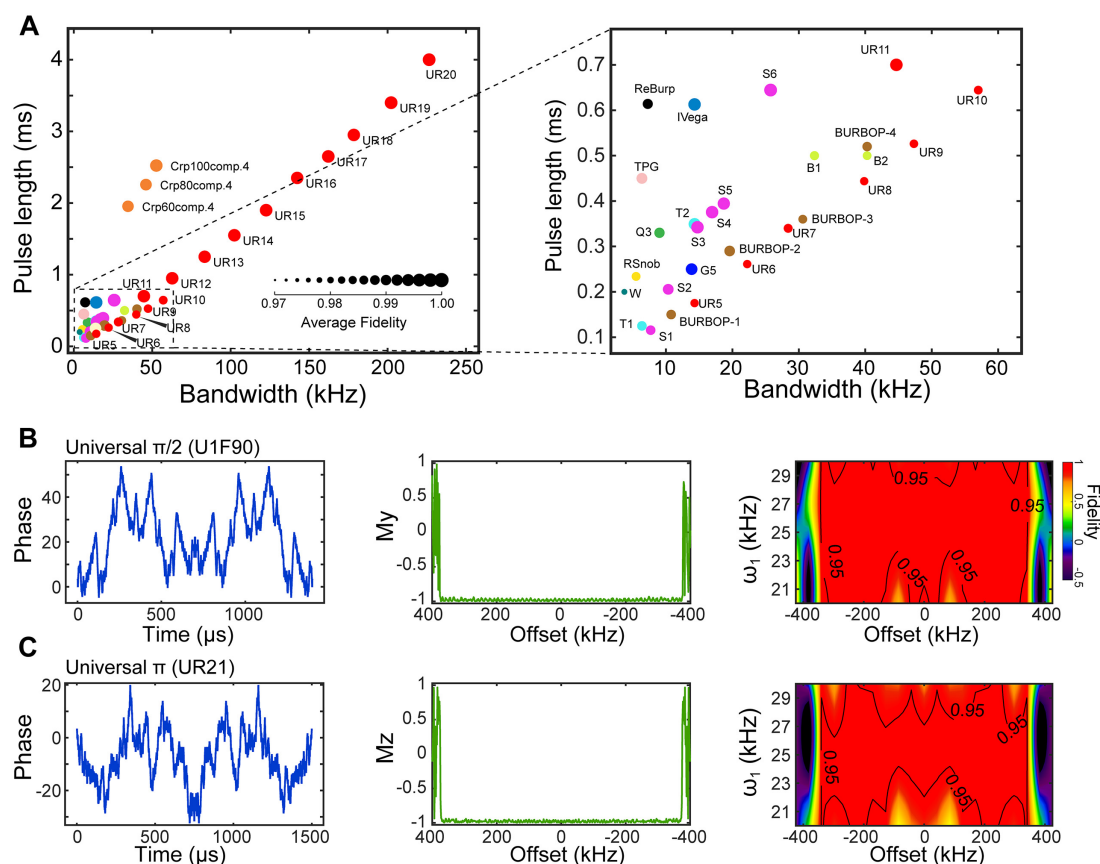
Figure 3. BB universal pulses and comparison of GENETICS-AI refocusing pulses with previously reported shapes. (A) Plot of the "Refocusing bandwidth-pulse length" for best performing GENETICS-AI pulses versus reported refocusing pulses. Refocusing BW of each pulse is calculated by averaging the offset responses of Mx and My magnetizations with a cutoff operational fidelity of 0.95. Each pulse is labeled with a short form and color-coded for the same family. Supplementary Table S2 shows the full names and relative reference for each pulse analyzed. The size of each dot represents the average operational fidelity of the pulse. Offset responses of a few selected RF shapes are shown in Figure S9. (B) Ultra-BB universal $\pi/2$ and (C), π pulse of BW 30 × ω_1. Amplitude shapes of these pulses are constant (ω_1) with phase shapes shown on the left. Offset response of π and $\pi/2$ are shown for initial states Mz (middle). Simulated fidelity response with offset and RF amplitude are shown on the right panel.

of 550 kHz with a pulse duration of 440 µs ($\omega_1 = 25$ kHz). We experimentally tested this BB pulse by recording a proton 1D spectrum of uniformly ^{15}N labeled K48C mutant of ubiquitin (U-^{15}N UBI^{K48C}) with an RF amplitude of 0.5 kHz on an 850 MHz spectrometer. The excitation BW of the pulse is 22 × 0.5 kHz = 11 kHz, sufficient for the excitation of the entire ^{1}H spectrum of a protein. A comparison between a rectangular pulse with ω_1 of 16.67 kHz and the BB pulse of 0.5 kHz is reported in Figure S15C. As expected, we observed a loss of signal intensity for the ultra-BB pulse due to the relaxation during the pulse execution. Nonetheless, the power required for these BB pulses is only 6.57 mW, while a corresponding rectangular pulse would require 7.3 W to excite the same BW. The latter shows that the algorithm has the potential to generate ultra low-power pulses for MRI, where power deposition becomes a problem for human subjects (9).

We then designed and applied BB pulses to multipulse NMR experiments. Specifically, we implemented BB $\pi/2$ and π pulses into the 2D [^{1}H-^{15}N] Heteronuclear Single Quantum Correlation (HSQC) pulse scheme, a central building block for biomolecular solution NMR spectroscopy (51–53). We first tested the tolerance of the BB pulses to RF inhomogeneity. Figure 4A shows the phase shapes of BB $\pi/2$ and π pulses designed to compensate for inhomogeneity in RF up to ±20% and an excitation BW covering the full chemical shift range of ^{1}H and ^{15}N for a Larmor frequency up to 1.2 GHz. The fidelity response of these pulses with offset and

RF amplitude is shown in Figure 4B. We compared the 2D spectra of the amide fingerprint of U-^{15}N UBI^{K48C} (54) acquired with the standard PFG-HSQC experiment (55, 56) with coherence selection and rectangular pulses and the corresponding BB GENETICS-AI version (GEN-HSQC). Figure 4C shows the 2D GEN-HSQC spectra recorded on U-^{15}N UBI^{K48C} with calibrated RF amplitudes of 12.5 and 5.8 kHz for ^{1}H and ^{15}N, respectively. To assess the BB pulses' tolerance for RF inhomogeneity on both ^{1}H and ^{15}N channels, we scaled the RF pulse amplitudes in steps of 5% up to ±20% while keeping their pulse duration constant. The insets of Figure 4C show the comparison of representative resonance intensities of the GEN-HSQC spectrum (I_{GEN}) versus the standard PFG-HSQC experiment (I_{RECT}). Overall, the spectrum acquired with the GEN-HSQC sequence displays higher S/N ratios, with a significantly higher tolerance for RF inhomogeneity across the entire spectrum. The gain in sensitivity observed with the GEN-HSQC sequence can be attributed to a combination of the high-fidelity pulse operation and RF inhomogeneity compensation. For PFG-HSQC, the intensity of the residues near the ^{1}H carrier frequency is ∼0.8 and drops to ∼0.5 for off-resonance irradiation relative to GEN-HSQC experiment. For amplitude attenuation of ±20%, the amide resonances in the PFG-HSQC are barely observable, whereas the signal intensities in the GEN-HSQC show a constant response. We performed the GEN-HSQC experiment on the catalytic subunit of cAMP-dependent protein kinase A (PKA-C, Figure 4D). For this
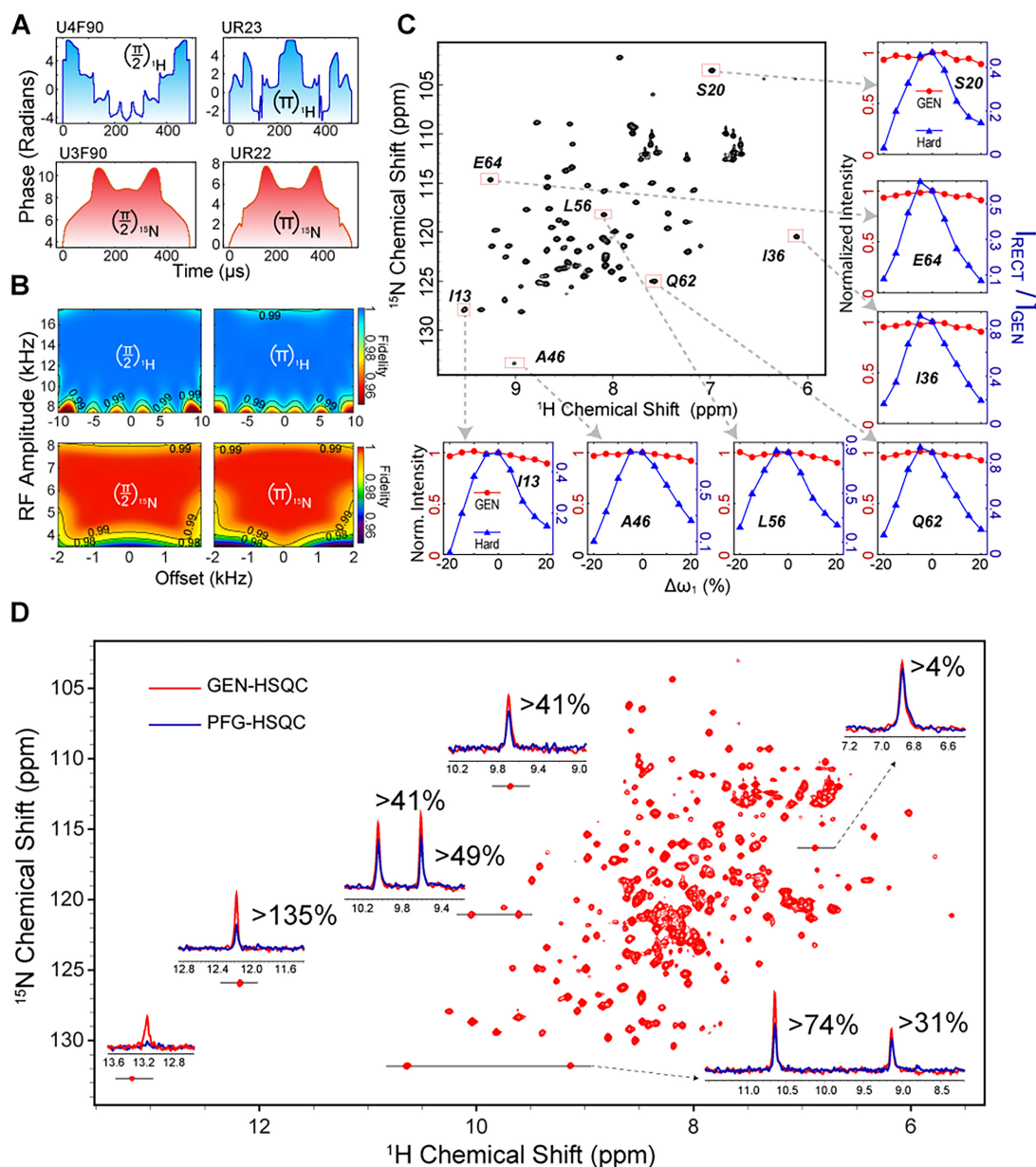
Figure 4. RF inhomogeneity compensated high-resolution multipulse NMR experiment. (A) GENETICS-AI shapes for universal π and $\pi/2$ pulses for ^{1}H (blue) and ^{15}N (red) channels. RF amplitudes were constant at 12.5 and 5.8 kHz for ^{1}H and ^{15}N channels, respectively. The pulse lengths for $\pi/2$ and π pulses were 488.6 and 509.8 μs for ^{1}H and 483.8 and 524 μs for ^{15}N. (B) Simulated fidelity response with offset and RF amplitude for ^{1}H (blue) and ^{15}N (red) for the pulse shapes in (A). The inner contour level indicates a fidelity of 0.99. (C) GENETICS-AI version of the HSQC (GEN-HSQC) spectrum of ^{15}N labeled K48C mutant of Ubiquitin recorded using calibrated amplitude values for ^{1}H (12.5 kHz) and ^{15}N (5.8 kHz) channels on a Bruker 850 MHz spectrometer at 300 K. The insets show the intensity comparison of the standard PFG-HSQC (using the Bruker pulse sequence—"hsqcetfpf3gpsi2") (I_{RECT}) and GEN-HSQC (I_{GEN}) at different RF amplitudes for selected residues. Left Y-axis shows the normalized peak intensities of standard (blue) and GEN-HSQC (red) relative to the calibrated reference spectra (I^0_{RECT} and I^0_{GEN}), whereas the right Y-axis represents the normalized intensity of standard HSQCs (blue) with respect to I^0_{GEN}. (D) GEN-HSQC spectra of 200 μM ^{15}N labeled catalytic subunit of protein kinase A (42 kDa). The figure insets compare the intensity of various resonances recorded using GEN-HSQC (red) and PFG-HSQC (blue) of the HSQC experiment. Both experiments are recorded on a Bruker 850 MHz spectrometer at 273 K using 128 complex indirect points were acquired with 16 scans per FID and a 1.5 s relaxation delay. Maximum RF amplitudes were 16.67 kHz for ^{1}H and 7.7 kHz for ^{15}N.

larger protein (42 kDa), the GEN-HSQC spectrum shows a higher S/N ratio and detects additional amide peaks that are not observable in the standard PFG-HSQC experiment. The drop in peak intensities observed in the PFG-HSQC experiment is due to the accumulation of pulse imperfections over multiple 180° pulses on both channels, i.e. five pulses for ^{1}H and four for ^{15}N. In fact, the GEN-HSQC experiment has a significantly higher RF inhomogeneity compensation relative to our previous implementation of

HSQC using the universal broadband pulse G5 (11). Lastly, we generated universal $\pi/2$ and π pulses for ^{1}H, ^{13}C, and ^{15}N nuclei for biomolecular NMR experiments up to 5 GHz (Figure S16). These RF pulses cover a BW of 20, 200, and 30 ppm for ^{1}H ($B_1 = 16.67$ kHz), ^{13}C ($B_1 = 16.67$ kHz), and ^{15}N ($B_1 = 5$ kHz) channels, respectively, for a static magnetic field $B_0 = 5$ GHz. Even at this high magnetic field, the average fidelity reached by these pulses is 0.999. Although this is a hypothetical scenario as the commercially
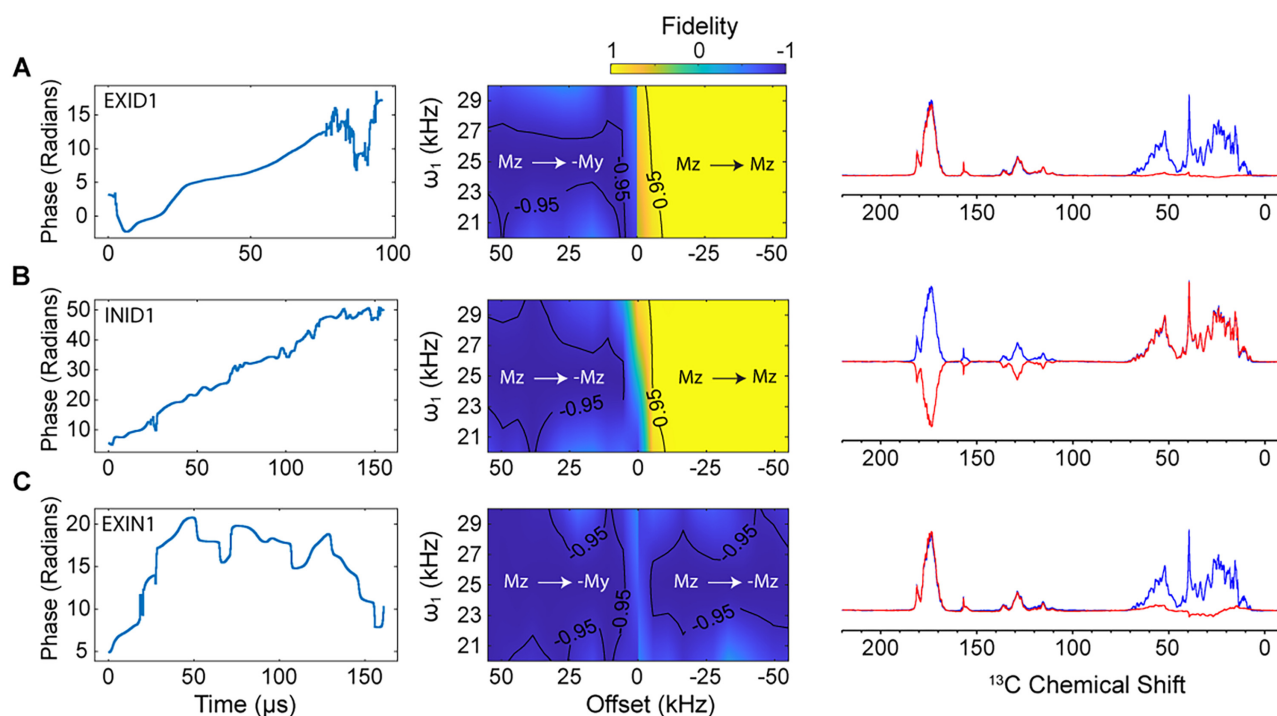
Figure 5. Band-selective excitation and inversion pulses with (A) excitation on the left half of BW and (B) Inversion on left half of the BW. Note that to observe M_z and $-M_z$, we added a reading pulse (90°) prior to acquisition. (C) Excitation on left half and inversion on right half of the BW, simultaneously. The excitation/inversion half of the offset response can be swapped by inverting the phase array. An RF amplitude of 25 kHz was used for the simulation. Experimental verification was performed using a uniformly ^{13}C labeled maltose binding protein (MBP) on an 850 MHz spectrometer. The band-selective excitation/inversion of aliphatic/carbonyl regions of the MBP are shown in the right column. The reference of the ^{13}C spectra is shown in blue, whereas the spectra obtained with different GENETICS-AI band-selective operations are shown in red.

available ultra-high magnetic fields are limited to 1.2 GHz, it shows that GENETICS-AI-generated pulses are suitable for biomolecular NMR spectroscopy at ultra-high magnetic fields greater than 1.2 GHz. Moreover, we generated new band-selective RF pulses for both excitation and inversion operations. These pulses are central to several triple-resonance experiments for liquid- or solid-state NMR techniques. However, the level of fidelity for the standard pulses is low, constituting a significant source of signal losses, particularly for multiple simultaneous operations (11, 56, 57). A typical application of selective excitation (or inversion) is the irradiation of ^{13}C carbonyl and aliphatic carbons resonances (58). Using GENETICS-AI, we generated selective pulses for excitation and inversion operations with a duration less than 1/4 of the traditional band-selective pulses (41, 59). The shapes and offset responses in terms of excitation (or inversion) regions of these band-selective excitation and inversion pulses are shown in Figure 5. We experimentally tested the pulses on the ^{13}C resonances of U-^{13}C labeled maltose-binding protein. From the 1D spectra, it is apparent that selective excitation (or inversion) occurs with almost no signal loss (Figure 5). Taken together, the simulations and experimental applications of BB and selective pulses designed by GENETICS-AI support their application to high and ultra-high magnetic field NMR spectroscopy on biomacromolecules.

Prototypical pulses for MRI

RF inhomogeneity represents a severe problem for MRI both at low and high magnetic fields, limiting both the resolution and sensitivity of images (9). In an effort to reduce RF inhomogeneity, we generated GENETICS-AI pulses for an SE imaging sequence, which is typically used for MRI experiments (4). Figure 6A shows the

RF inhomogeneity-compensated SE sequence (GEN-SE), where $\pi/2$ and π were substituted with the GENETICS-AI pulses. The pulse shapes and their fidelity response with offset and RF amplitude are shown in Figure S17. As a phantom, we utilized two 4 mm glass beads into a 5 mm Shigemi® tube filled with a solution of 10% H_2O and 90% ^2H_2O (Figure 6B). We then generated 1D images of the phantom along the Z-direction using the SE sequence with standard rectangular-shaped pulses and compared them with the GEN-SE sequence (Figure 6C). To simulate the effect of RF inhomogeneity, we scaled the RF pulse amplitudes up to ±100%, keeping the pulse length constant. The intensity of the images acquired with the standard rectangular pulses becomes significantly lower with scaling the RF amplitude (Figure 6D). In contrast, the GEN-SE creates high-quality images with fewer artifacts, even at ω_1 inhomogeneity of ±80% (Figure 6E) (60). Overall, these tests show a superior tolerance of the GENETICS-AI pulses to RF field inhomogeneity than the rectangular pulses, making them more suitable for in vivo imaging and spectroscopy as well as for analyzing materials.

The first application of artificial neural networks to pulse design was pioneered by Gezelter and Freeman, who trained a basic algorithm and generated JANUS pulses able to create antiphase × magnetization (61). More recently, deep reinforcement learning or neural networks have been used to optimize and refine RF pulse shapes for imaging (62–65). In contrast, GENETICS-AI generates pulse shapes for general spin operations with customizable BW, inhomogeneity compensation, and fidelity. Notably, during the execution of the GENETICS-AI pulses, there is no chemical shift evolution (Figure S19), and the final state of magnetization is unaffected by J-coupling (Figure S20). The GENETICS-AI-generated pulses possess smooth phase shapes and constant
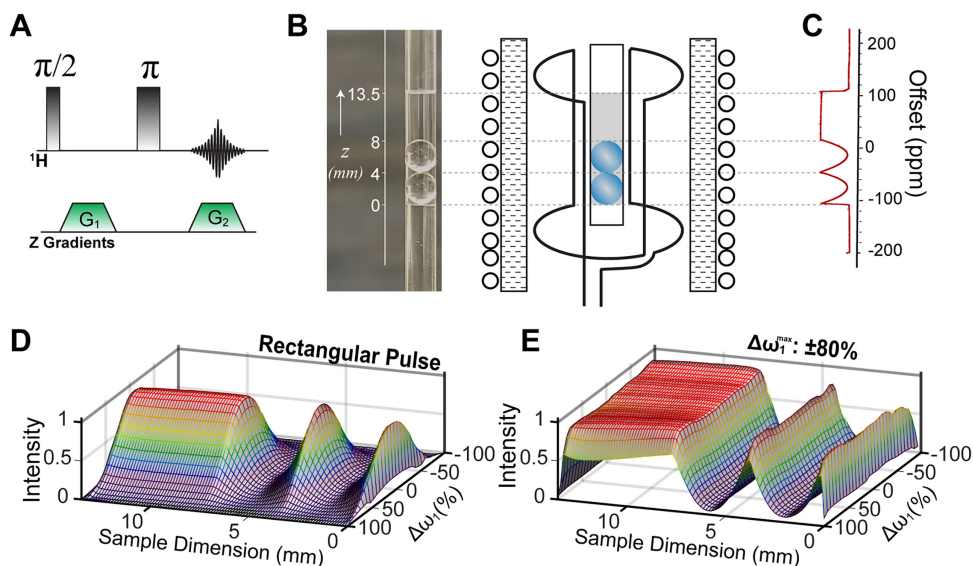
Figure 6. SE imaging under ultra-high RF inhomogeneity. (A) SE pulse sequence used for imaging. The $\pi/2$ and π pulses are replaced with GENETICS-AI pulses for GEN-SE sequence. The amplitude of the pulses is constant (16.67 kHz) and pulse lengths for $\pi/2$ and π pulses are 437 and 567 μs, respectively. The maximum RF amplitude tolerance level ($\Delta\omega_1^{max}$) of these pulses were ±80%. The gradient strengths (G_1 and G_2) for all the experiments were set at 50% (3.3 G cm^{-1}). (B) Diagram of phantom and coil geometry. The phantom consists of two glass beads of diameter 4 mm in a 5 mm Shigemi tube filled with 10% D_2O and 90% H_2O. (C) 1D image of the phantom using the pulse sequence in (A). (D) RF inhomogeneity response of 1D imaging using standard rectangular-shaped pulses of amplitude 16.67 kHz. (E) Same as (D) using GENETICS-AI pulses. The RF shapes and their fidelity profiles are shown in Figure S17. The experiments were performed in a Bruker 900 MHz NMR spectrometer.

amplitude, thanks to the neural network trained on an extensive library of realistic high-fidelity RF shapes and performance profiles. The forward and reverse optimization algorithms coupled with a neural network generate time-optimal phase shapes in a matter of milliseconds. Unlike all previously reported pulse shapes, the operational fidelity, BW, RF inhomogeneity compensation, and flip angle of the new pulses are customizable and enable the user to meet the requirements of various magnetic resonance applications. Remarkably, we generated BB pulses suitable for high and ultra-high magnetic field spectroscopy. We also reached a high level of control for the spin dynamics in multipulse NMR experiments, which involve large ensembles of nuclear spin quantum processors in a highly mixed state. At this time, the GENETICS-AI algorithm can design only pulses with constant amplitude or preselected amplitude shapes. Future developments will include coding the RF pulse amplitude in the search space. The latter will potentially improve the design of band-selective pulses, minimizing the power required for specific operations.

In conclusion, we showed that combining an evolutionary algorithm and AI makes it possible to control the spin dynamics with high fidelity and design inhomogeneity compensated RF pulses directly applicable to NMR, MRI, and quantum computing. The proof-of-concept applications illustrated here lay the groundwork for more complex implementations of AI-driven RF design. These technical advancements will impact several fields, including structural biology, biomedicine, material sciences, and quantum information.

Experimental section
Architecture of GENETICS-AI

The architecture of GENETICS-AI is reported in Figure S1. Input module: The first module consists of a customizable input inter-

face in which the user defines the specific problem to be solved. The input parameters are as follows:

- Operator type: desired pulse operation, i.e. excitation, inversion, universal π, $\pi/2$, $\pi/3$, and $\pi/4$ pulses;
- Maximum RF amplitude: maximum allowed peak amplitude of the shape;
- Operational BW: desired BW for the pulse operation (kHz);
- RF amplitude compensation level: amount of RF inhomogeneity/miscalibration to be compensated;
- Average fidelity for the operation: average fidelity for the pulse, where the average is calculated over the range of specified BW and/or amplitude compensation level.

Iterative Forward Search and Self Correction Algorithms (IFSA-ISCA): generation of OPS

The first part of the algorithm consists of novel iterative optimization algorithms called IFSA and ISCA that perform optimal conversion of a resource into a target variable, generating a family of solutions, i.e. optimal phase surface or OPS. The resource variable provides the range of maximum RF amplitude or pulse length for the IFSA-ISCA to explore. In contrast, the target variable is set according to the problem type, such as operational BW, fidelity, and compensation levels for various inhomogeneities. The individual solutions in OPS are interconnected through the iterative forward and backward optimization network of IFSA-ISCA. These algorithms' primary objective is to maintain a minimum fitness value for the optimization network by altering the variable's value outside the optimal space and performing further optimization. For the BB pulse design, the operational BW and total nutation angle (Θ) are the target and resource variables. Θ is the time integral of magnitude of RF field ($|\omega_1|$) shape over the pulsing time. IFSA initializes these variables using the standard rectangular-shaped pulse BW and nutation angle, which is

the minimum possible value for the resource variable. After initialization, IFSA performs an adiabatic perturbation of the target variable, which results in a loss of the fitness value. IFSA maintains a minimum fitness value through an iterative loop by increasing the resource variable, followed by an optimization step. IFSA increases the degree of optimization through an iterative perturbation-evolution process and finds optimal solutions virtually impossible to reach using a standard optimization algorithm. The iterative evolution process is always monitored to check the fitness of the solutions, and a backward evolution is initiated if necessary. This perturbation-evolution process with forward and backward searches connects each family's solution either as a generator or corrector. To illustrate IFSA-ISCA protocol, let us consider the case of a 100-point BB inversion pulse design (Figure S2A). ISCA optimization is initialized with BW and Θ of a standard rectangular π pulse. The algorithm performs the first iteration by perturbing the BW by ε. The small increase in BW reduces the fitness value of the RF shape. At this point, IFSA tries to maintain the fitness of the shape by increasing Θ, a step which is followed by Broyden–Fletcher–Goldfarb–Shanno (BFGS) (66) or a Genetic Algorithm (GA) optimization (67). This optimization step evolves the RF shape to a new "perturbed" BW and updates the fitness value. Once IFSA-ISCA attains a cutoff fitness value, BW will be perturbed again and undergoes the same optimization process. The evolution of broadband pulse is monitored by "Θ–BW" plot (Figure S2B). The forward search of IFSA is coupled with a self-correction protocol that initiates an ISCA to keep the time-optimal trajectory. Once initiated, ISCA performs reverse iterations by reducing Θ in small steps. As in the IFSA case, the system compensates for the loss in fitness by reducing bandwidth by ε. Once the system reaches the fidelity cutoff, the iterative reverse search continues until the reverse trajectory meets the forward (Figure S2B). This adiabatic transition of optimal RF shape from low to high BW continues until the IFSA-ISCA reaches the maximum BW imposed by the digital resolution of the pulse shape (Figure S12). The self-correcting protocol is based on a simple philosophy that if the nth step's fidelity is more than expected, the previous steps may not be time optimal. Therefore, the self-correcting protocol is triggered when IFSA detects an increase in fitness, typically 20% close to the maximum from cutoff in one optimization step. The latter indicates a possible correction in the trailing trajectory, and ISCA updates this with a higher slope trajectory. Every BFGS/GA optimization initiate with an RF shape obtained from the previous iteration of both forward and reverse searches. This initial guess considerably speeds up the optimization procedure and maintains a smooth transition of the shape with the target variable. As shown in Figure S18, we obtained a smooth phase surface for a 200-point universal π pulse and inversion pulse. This semi-continuous solution surface with increasing BW is the OPS. OPS's geometric features increase with operational complexity, BW, average fidelity, and RF amplitude (ω_1), compensation level (Figure S12). OPS for 1,000-point inversion and 2,000-point universal π pulse for higher BWs are shown in Figure S13. The fitness function ($\bar{\mathcal{F}}$) used in IFSA-ISCA is defined as the average operational fidelity of a given RF shape, and is calculated over a range of offset and $\Delta\omega_1$:

$$\bar{\mathcal{F}} = \frac{1}{N_{BW}N_{\Delta\omega_1}} \sum_{BW}\sum_{\Delta\omega_1} Trace\left(U_{tar}\cdot U_{pul}^{\dagger}\right), \qquad (2)$$

where U_{tar} is the target unitary operator, U_{pul} is the unitary operator of the RF shape, N_{BW} is the number of offset values from -BW/2 to +BW/2 used in the averaging, and $N_{\Delta\omega_1}$ is the number of RF am-

plitudes from ($\omega_1 - \Delta\omega_1/2$) to ($\omega_1 + \Delta\omega_1/2$) used in the averaging. Even though higher values of N_{BW} and $N_{\Delta\omega_1}$ improve the fitness, smaller values are generally preferred as they are less computationally expensive. An example target unitary operator for universal π pulse is $U_{tar} = e^{-i\pi I_x}$. The fitness function given in equation (2) is used for operator optimization, where the operator type is a unitary operator. The fitness function for a state preparation (such as excitation and inversion) pulse design is given by

$$\bar{\mathcal{F}} = \frac{1}{N_{BW}N_{\Delta\omega_1}} \sum_{BW}\sum_{\Delta\omega_1} Trace\left(\rho_{tar}\cdot U_{pul}\cdot \rho_{ini}\cdot U_{pul}^{\dagger}\right), \qquad (3)$$

where ρ_{ini} and ρ_{tar} are the initial and target states, respectively. For the inversion pulse, the initial state corresponds to $\rho_{ini} = I_z$, and the target state is $\rho_{tar} = -I_z$.

Neural Network (PhaseNET): Generation of new optimal solutions from the OPS library

Extracting a specific pulse shape with desired properties from the OPS library is computationally challenging. Therefore, we used the AI module coded in MATLAB® to speed up the selection of the best phase shape and generate solutions that are not part of the original OPS library. Once IFSA-ISCA generates the OPS library, all the shapes are indexed using the "Contour Indexing Algorithm" (CIA). CIA evaluates all the possible rectangles fit within the various contour levels of the "offset-$\Delta\omega_1$" pulse profile, as shown in Figure S3A. The index values of each RF shape (CIA files) and the corresponding shape are used for training the neural network (PhaseNET), which predicts new RF shapes that are not directly available in the OPS library. To accomplish this task, we used the *traincgp* function provided in MATLAB (Conjugate gradient back-propagation with Polak–Ribiére updates). A schematic of PhaseNET is reported in Figure S3B. The validation of each shape from the PhaseNET is performed by simulating the responses of the RF pulse predicted by the trained neural network. If the fidelity, BW, and inhomogeneity compensation match the requirements, PhaseNET outputs a new shape in the specified format. In the case of the arbitrary flip angle generator, the PhaseNET was validated by evaluating the RF shapes for different flip angles using 1,000 different runs. For each run, the algorithm found the optimal solution for the specified RF shape.

All GENETICS-AI algorithms are written in MATLAB® (R2018a) and executed on a personal computer with Intel® Core™ i7-7700 K processor. The generation of a single OPS of 100 points takes approximately 12 hours of calculation on a single core. For a 500-point shape, the calculation time grows exponentially to approximately a week of computer time. So far, we implemented up to 2,000-point RF shape, generating a database with more than 2,00,000 RF shapes for various operators, BWs, and RF inhomogeneity compensation levels.

The details of the GENETICS-AI software can be found at: https://patentcenter.uspto.gov/#!/applications/16861506/ifw/docs.

NMR sample preparations

For the spin entanglement experiments, neat ^{13}C labeled chloroform ($^{13}CHCl_3$) was added to a solution of $CDCl_3$ (1:10 ratio) and loaded into a 5 mm Shigemi® tube. Two qubit quantum states of ^1H and ^{13}C spins were measured using quantum state tomography, as explained in Mitra et al. (37). All experiments were recorded on a Bruker 600 MHz spectrometer at 290 K.

Recombinant expression and purification of U-^{15}N ubiquitin K48C mutant (UbiK^{48C}) were carried out as described previously (68). The sample consisted of 0.80 mg of U-^{15}N UbiK^{48C} was

solubilized in 10 mM sodium acetate buffer (pH 6.0) and 100 mM NaN_3. The final concentration of the sample was 500 μM. All experiments were performed on a Bruker 850 MHz spectrometer at 300 K.

The catalytic subunit of PKA (PKA-C, Mus musculus gene) was expressed in *Escherichia coli* BL21 (DE3) cells in M9 minimal medium at 24°C. After cell lysis, PKA-C purification was carried out with affinity chromatography using the His6-RIIa(R213K) subunit (Hemmer et al., 1997). The pellets of cell overexpressing Rlla (R213K) and PKA-C were combined and suspended in a buffer containing 30 mM 3-(N-morpholino) propane sulfonic acid (MOPS), 200 μM ATP, 15 mM $MgCl_2$, 0.15 mg mL^{-1} lysozyme, 1 mM PMSF; 100 U mL^{-1} DNAse I (Roche Applied Science), and 5 mM 2-mercaptoethanol (pH 8.0). The cells were lysed using a French press at 1,000 psi. After centrifugation, the supernatant was added to a slur of Ni^{+2}-NTA nitrilotriacetic acid resin (Thermo Scientific, 1 mL of resin per liter of culture) and shaken at 4°C for approximately 3 hours. After washing the resin with 30 mM MOPS, 25 mM KCl, 15 mM $MgCl_2$, and 5 mM 2-mercaptoethanol (pH 8.0), PKA-C was eluted using 30 mM MOPS, 25 mM KCl, 15 mM $MgCl_2$, 5 mM 2-mercaptoethanol, and 1 mM cAMP (pH 8.0). The fractions containing PKA-C were collected and dialyzed overnight in 20 mM KH_2PO_4, 25 mM KCl, and 5 mM 2-mercaptoethanol (pH 6.5). Cation exchange chromatography was performed using a HiTrap SP column (GE Healthcare Life Sciences) to separate the different phosphorylated isoforms of PKA-C. A linear gradient of KCl in 20 mM KH_2PO_4 at pH 6.5 (Yonemoto et al., 1993) was applied, and the purified protein was collected and stored in phosphate buffer with 10 mM DTT, 10 mM, MgCl2, and 1.0 mM NaN3, at 4°C. For perdeuterated protein expression, the cells were growth 80% ^2H_2O in M9 minimal medium using a 2.0 L fermenter. The most abundant isoform of PKA-C, corresponding to phosphorylation at S338, T197, and S10 residues (isoform II) (Walsh and Ashby, 1973), was utilized for acquiring the NMR experiments.

MBP was expressed in *E. coli* BL21 DE3 cells (NEB) containing the pMAL plasmid. After an overnight growth in LB media, the cells were spun down and resuspended in M9 media in 100% ^2H_2O with $^{15}NH_4Cl$ as the only source of nitrogen. MBP expression was induced at an OD_{600} of 0.8 using isopropyl β-D-1-thiogalactopyranoside (IPTG). Upon reaching an OD of ∼5, the cells were harvested and lysed in a buffer containing 20 mM phosphate buffer (PBS), 120 mM NaCl, 1 mM EDTA, mM 0.15 mg mL^{-1} lysozyme, 0.05% glycerol, 2 mM dithiothreitol (DTT), one tablet of protease inhibitor (cOmplete™, Roche Applied Science), and 100 U mL^{-1} DNAse I (Roche Applied Science). Amylose resin (NEB) was added to the supernatant and stirred overnight. After washing with a buffer containing 20 mM PBS, 120 mM NaCl, and 1 mM EDTA, the resin was loaded into a mini-column, and MBP was eluted using 60 mM maltose. The elution containing MBP was concentrated and loaded into a size exclusion Superdex 200 (GE Healthcare Life Sciences) to eliminate impurity. The correct mass was assessed using mass spectrometry. The final sample consisted of 1 mM MBP in 10 mM Na_2HPO_4, 0.1 mM EDTA, and 1 mM NaN_3 buffer. The PFG-HSQC and GEN-HSQC experiments were collected on a Bruker 850 MHz spectrometer at 300 K.

Acknowledgments

Supplementary Material

Supplementary material is available at *PNAS Nexus* online.

Funding

Authors' Contributions

M.V.S and G.V. designed the research. M.V.S. wrote the code. M.V.S., K.P., and C.O. performed the experiments. G.V. and M.V.S. analyze the data. All authors contributed to writing and reviewing the paper.

Data Availability

All RF shapes and pulse sequences are publicly available through the University of Minnesota repository site: https://doi.org/10.130 20/f9pb-ma04 and GitHub https://github.com/manuvsub/GENE TICSAI.

References

1. Nielsen MA, Chuang IL. 2010. Quantum computation and quantum information: 10th anniversary edition. Cambridge (MA): Cambridge University Press.
2. Ernst RR, Bodenhausen G, Wokaun A. 1987. Principles of nuclear magnetic resonance in one and two dimensions. Oxford: Clarendon Press.
3. Xu X, *et al.* 2007. Coherent optical spectroscopy of a strongly driven quantum dot. Science. 317(5840):929–932.
4. Brown RW, Cheng YCN, Haacke EM, Thompson MR, Venkatesan R. 2014. Magnetic resonance imaging: physical principles and sequence design. New York (NY): John Wiley & Sons.
5. Warren WS, Rabitz H, Dahleh M. 1993. Coherent control of quantum dynamics: the dream is alive. Science. 259(5101): 1581–1589.
6. Levitt MH. 1986. Composite pulses. Prog Nucl Magn Reson Spectrosc. 18(2):61–122.
7. Manu VS, Kumar A. 2014. Quantum simulation using fidelity-profile optimization. Phys Rev A. 89(5):052331.
8. Dolde F, *et al.* 2014. High-fidelity spin entanglement using optimal control. Nat Commun. 5:3371.
9. Ladd ME, *et al.* 2018. Pros and cons of ultra-high–field MRI/MRS for human application. Prog Nucl Magn Reson Spectrosc. 109:1–50.
10. Ardenkjaer-Larsen JH, *et al.* 2015. Facing and overcoming sensitivity challenges in biomolecular NMR spectroscopy. Angew Chem Int Ed. 54(32):9162–9185.
11. Xia Y, *et al.* 2017. Enhancing the sensitivity of multidimensional NMR experiments by using triply-compensated π pulses. J Biomol NMR. 69(4):237–243.
12. Garwood M, DelaBarre L. 2001. The return of the frequency sweep: designing adiabatic pulses for contemporary NMR. J Magn Reson. 153(2):155–177.
13. Khaneja N, Reiss T, Kehlet C, Schulte-Herbruggen T, Glaser SJ. 2005. Optimal control of coupled spin dynamics: design of NMR pulse sequences by gradient ascent algorithms. J Magn Reson. 172(2):296–305.

14. Fortunato EM, *et al.* 2002. Design of strongly modulating pulses to implement precise effective Hamiltonians for quantum information processing. J Chem Phys. 116(17):7599–7606.

15. Freeman R. 1998. Shaped radiofrequency pulses in high resolution NMR. Prog Nucl Magn Reson Spectrosc. 32(1):59–106.

16. Kupce E, Boyd J, Campbell ID. 1995. Short selective pulses for biochemical applications. J Magn Reson B. 106(3):300–303.

17. Abramovich D, Vega S. 1993. Derivation of broadband and narrowband excitation pulses using the Floquet formalism. J Magn Reson A. 105(1):30–48.

18. McCoy MA, Mueller L. 1992. Selective shaped pulse decoupling in NMR: homonuclear [carbon-13]carbonyl decoupling. J Am Chem Soc. 114(6):2108–2112.

19. Coote P, Anklin C, Massefski W, Wagner G, Arthanari H. 2017. Rapid convergence of optimal control in NMR using numerically-constructed toggling frames. J Magn Reson. 281:94–103.

20. Somai V, Wright AJ, Fala M, Hesse F, Brindle KM. 2020. A multi spin echo pulse sequence with optimized excitation pulses and a 3D cone readout for hyperpolarized (13) C imaging. Magn Reson Med. 84(4):1895–1908.

21. Harris KJ, Lupulescu A, Lucier BE, Frydman L, Schurko RW. 2012. Broadband adiabatic inversion pulses for cross polarization in wideline solid-state NMR spectroscopy. J Magn Reson. 224:38–47.

22. Li JS, Ruths J, Yu TY, Arthanari H, Wagner G. 2011. Optimal pulse design in quantum control: a unified computational method. Proc Natl Acad Sci U S A. 108(5):1879–1884.

23. Theis T, Feng Y, Wu T, Warren WS. 2014. Composite and shaped pulses for efficient and robust pumping of disconnected eigenstates in magnetic resonance. J Chem Phys. 140(1): 014201.

24. Pauly J, Roux PL, Nishimura D, Macovski A. 1991. Parameter relations for the Shinnar-Le Roux selective excitation pulse design algorithm (NMR imaging). IEEE Trans Med Imaging. 10(1): 53–65.

25. Conolly S, Nishimura D, Macovski A. 1986. Optimal control solutions to the magnetic resonance selective excitation problem. IEEE Trans Med Imaging. 5(2):106–115.

26. Rund A, Aigner CS, Kunisch K, Stollberger R. 2018. Magnetic resonance RF pulse design by optimal control with physical constraints. IEEE Trans Med Imaging. 37(2):461–472.

27. Xu D, King KF, Zhu Y, McKinnon GC, Liang ZP. 2008. Designing multichannel, multidimensional, arbitrary flip angle RF pulses using an optimal control approach. Magn Reson Med. 59(3):547–560.

28. Vinding MS, Maximov II, Tosner Z, Nielsen NC. 2012. Fast numerical design of spatial-selective RF pulses in MRI using Krotov and quasi-Newton based optimal control methods. J Chem Phys. 137(5):054203.

29. Shang H, *et al.* 2016. Multiband RF pulses with improved performance via convex optimization. J Magn Reson. 262:81–90.

30. Shor PW. 1994. Algorithms for quantum computation: discrete logarithms and factoring. Proceedings 35th Annual Symposium on Foundations of Computer Science, p. 124–134.

31. Bennett CH, DiVincenzo DP. 2000. Quantum information and computation. Nature. 404(6775):247–255.

32. Warren WS. 1997. The usefulness of NMR quantum computing. Science. 277(5332):1688–1690.

33. Cory DG, Fahmy AF, Havel TF. 1997. Ensemble quantum computing by NMR spectroscopy. Proc Natl Acad Sci U S A. 94(5):1634–1639.

34. Suter D, Mahesh TS. 2008. Spins as qubits: quantum information processing by nuclear magnetic resonance. J Chem Phys. 128(5):052206.

35. Oliveira IS, Bonagamba TJ, Sarthour RS, Freitas JCC, deAzevedo ER, editors. 2007. 6-Entanglement in liquid-state NMR. NMR quantum information processing. Amsterdam: Elsevier Science B.V. p. 207–220.

36. Manu VS, Veglia G. 2015. Genetic algorithm optimized triply compensated pulses in NMR spectroscopy. J Magn Reson. 260:136–143.

37. Mitra A, Ghosh A, Das R, Patel A, Kumar A. 2005. Experimental implementation of local adiabatic evolution algorithms by an NMR quantum information processor. J Magn Reson. 177(2):285–298.

38. Jones JA. 2003. Robust Ising gates for practical quantum computation. Phys Rev A. 67(1):012317.

39. Zlatanov KN, Vitanov NV. 2020. Generation of arbitrary qubit states by adiabatic evolution split by a phase jump. Phys Rev A. 101(1):013426.

40. DiVincenzo DP. 2000. The physical implementation of quantum computation. Fortschr Phys. 48(9–11):771–783.

41. Cavanagh J, Fairbrother WJ, Palmer AG, Rance M, Skelton NJ. 2007. Protein NMR spectroscopy: principles and practice, 2nd ed. Cambridge, MA: Academic Press. p. 1–888.

42. Emsley L, Bodenhausen G. 1992. Optimization of shaped selective pulses for NMR using a quaternion description of their overall propagators. J Magn Reson. 97(1):135–148.

43. Tycko R, Cho HM, Schneider E, Pines A. 1985. Composite pulses without phase distortion. J Magn Reson. 61(1):90–101.

44. Shaka AJ, Pines A. 1987. Symmetric phase-alternating composite pulses. J Magn Reson. 71(3):495–503.

45. Kobzar K, Ehni S, Skinner TE, Glaser SJ, Luy B. 2012. Exploring the limits of broadband 90° and 180° universal rotation pulses. J Magn Reson. 225:142–160.

46. Boeszoermenyi A, *et al.* 2019. Aromatic (19)F–(13)C TROSY: a background-free approach to probe biomolecular structure, function, and dynamics. Nat Methods. 16(4):333–340.

47. Zheng A, Liu S-B, Deng F. 2017. 31P NMR chemical shifts of phosphorus probes as reliable and practical acidity scales for solid and liquid catalysts. Chem Rev. 117(19):12475–12531.

48. Stannarius R. 2017. Magnetic resonance imaging of granular materials. Rev Sci Instrum. 88(5):051806.

49. Bray JM, *et al.* 2020. Operando visualisation of battery chemistry in a sodium-ion battery by 23Na magnetic resonance imaging. Nat Commun. 11(1):2083.

50. Kay LE. 2019. Artifacts can emerge in spectra recorded with even the simplest of pulse schemes: an HMQC case study. J Biomol NMR. 73(8–9):423–427.

51. Palmer AG, Cavanagh J, Wright PE, Rance M. 1991. Sensitivity improvement in proton-detected two-dimensional heteronuclear correlation NMR spectroscopy. J Magn Reson. 93(1):151–170.

52. Schleucher J, *et al.* 1994. A general enhancement scheme in heteronuclear multidimensional NMR employing pulsed field gradients. J Biomol NMR. 4(2):301–306.

53. Kay L, Keifer P, Saarinen T. 1992. Pure absorption gradient enhanced heteronuclear single quantum correlation spectroscopy with improved sensitivity. J Am Chem Soc. 114(26):10663–10665.

54. Liu Z, *et al.* 2012. Noncovalent dimerization of ubiquitin. Angew Chem Int Ed Engl. 51(2):469–472.

55. Bax A, Pochapsky SS. 1992. Optimized recording of heteronuclear multidimensional NMR spectra using pulsed field gradients. J Magn Reson. 99(3):638–643.

56. Muhandiram DR, Kay LE. 1994. Gradient-enhanced triple-resonance three-dimensional NMR experiments with improved sensitivity. J Magn Reson B. 103(3):203–216.

57. Wittekind M, Mueller L. 1993. HNCACB, a high-sensitivity 3D NMR experiment to correlate amide-proton and nitrogen resonances with the alpha- and beta-carbon resonances in proteins. J Magn Reson B. 101(2):201–205.

58. Grzesiek S, Bax A. 1992. An efficient experiment for sequential backbone assignment of medium-sized isotopically enriched proteins. J Magn Reson. 99(1):201–207.

59. Emsley L, Bodenhausen G. 1990. Gaussian pulse cascades: new analytical functions for rectangular selective inversion and in-phase excitation in NMR. Chem Phys Lett. 165(6):469–476.

60. Truong T-K, Chakeres DW, Beversdorf DQ, Scharre DW, Schmalbrock P. 2006. Effects of static and radiofrequency magnetic field inhomogeneity in ultra-high field magnetic resonance imaging. Magn Reson Imaging. 24(2):103–112.

61. Gezelter JD, Freeman R. 1990. Use of neural networks to design shaped radiofrequency pulses. J Magn Reson. 90(2):397–404.

62. Vinding MS, Skyum B, Sangill R, Lund TE. 2019. Ultrafast (milliseconds), multidimensional RF pulse design with deep learning. Magn Reson Med. 82(2):586–599.

63. Ilott AJ, Mohammadi M, Chang HJ, Grey CP, Jerschow A. 2016. Real-time 3D imaging of microstructure growth in battery cells using indirect MRI. Proc Natl Acad Sci. 113(39):10779.

64. Shin D, *et al.* 2021. Deep reinforcement learning-designed radiofrequency waveform in MRI. Nat Mach Intell. 3(11):985–994.

65. Shin D, *et al.* 2020. Deep reinforcement learning designed Shinnar-Le Roux RF pulse using root-flipping: DeepRFSLR. IEEE Trans Med Imaging. 39(12):4391–4400.

66. Kelley CT. 1999. Iterative methods for optimization. Philadelphia, PA: SIAM.

67. Holland JH. 1992. Adaptation in natural and artificial systems: an introductory analysis with applications to biology, control, and artificial intelligence. Cambridge (MA): MIT Press.

68. Olivieri C, *et al.* 2018. Simultaneous detection of intra- and inter-molecular paramagnetic relaxation enhancements in protein complexes. J Biomol NMR. 70(3):133–140.